Optimization-based strategies for the operation of low-density polyethylene tubular reactors: Moving horizon estimation

Victor M. Zavala *, Lorenz T. Biegler

Department of Chemical Engineering, Carnegie Mellon University, 5000 Forbes Avenue, Pittsburgh, PA 15213, USA

ABSTRACT

We present a moving horizon estimation (MHE) application for multi-zone low-density (LDPE) polyethylene tubular reactors. The strategy incorporates a first-principles dynamic model comprised of large sets of nonlinear partial, differential and algebraic equations (PDAEs). It was found that limited temperature measurements distributed along the reactor are sufficient to infer all the model states in space and time and to track uncertain time-varying phenomena such as fouling. A full discretization strategy and a state-of-the-art nonlinear programming (NLP) solver are used to enable the computational feasibility of the approach. It is demonstrated that the MHE estimator exhibits fast performance and is well suited for applications of industrial interest.

Published by Elsevier Ltd.

1. Motivation and background information

Low-density polyethylene (LDPE) is an important commodity polymer in today's economy due to its high flexibility and relatively low-cost (Knuuttila, Lehtinen, & Nummila-Pakarinen, 2004). LDPE is mostly produced in tubular reactors by free-radical polymerization of ethylene at supercritical conditions (2000–3000 atm and 150–350 °C). A typical tubular reactor and corresponding temperature profiles for the reactor core and jackets are sketched in Fig. 1. This type of reactor consists of long pipes (1–3 km) with small inner diameters (5–10 cm) and thick reactor walls (2–5 cm) which are divided into several reaction and cooling zones. Each zone is equipped with a jacket cooling system used to remove the large amounts of heat produced by polymerization. Multiple side streams containing monomer, comonomer, chain transfer agent (CTA) and initiators can be fed along the reactor to control the temperature profile and the resulting polymer properties. The large heat transfer areas and low degrees of back-mixing resulting in these units permit the high throughput production of LDPE resins with unique processability and end-use properties.

Despite the multiple benefits offered by LDPE tubular reactors, there exist several factors limiting their performance. The first issue arises due to their distributed and multivariable nature which gives rise to complex interactions along the pipe. The most common approach to cope with this complexity is to find feasible operating conditions able to produce a particular grade by trial and error and/or experience. The resulting operating recipes are enforced strictly through an appropriate regulatory control system. While these recipes work well in many cases, they tend to be rather conservative and need to be constantly adapted for each new grade incorporated into the product portfolio. A second important problem arising in LDPE reactors is the persistent and slow deposition of polymer on the inner reactor walls (Buchelli et al., 2005a,b; Lacunza, Ugrin, Brandolin, & Capiati, 1998). The resulting fouling layer is highly insulating and severely decreases the heat-transfer rate to the cooling jacket. Since the polymerization reactions are highly exothermic, the production rate needs to be dropped progressively in order to keep the temperature profile within safe limits and avoid thermal runaway. The impact of fouling on the overall profitability of high-throughput LDPE reactors is extremely large.

The potential economic benefits and high operational complexity of LDPE reactors have motivated research efforts in many areas. Extensive experimental studies have been performed in order to understand the fundamental interactions between the reactor

* Corresponding author. Tel.: +1 412 268 2238.
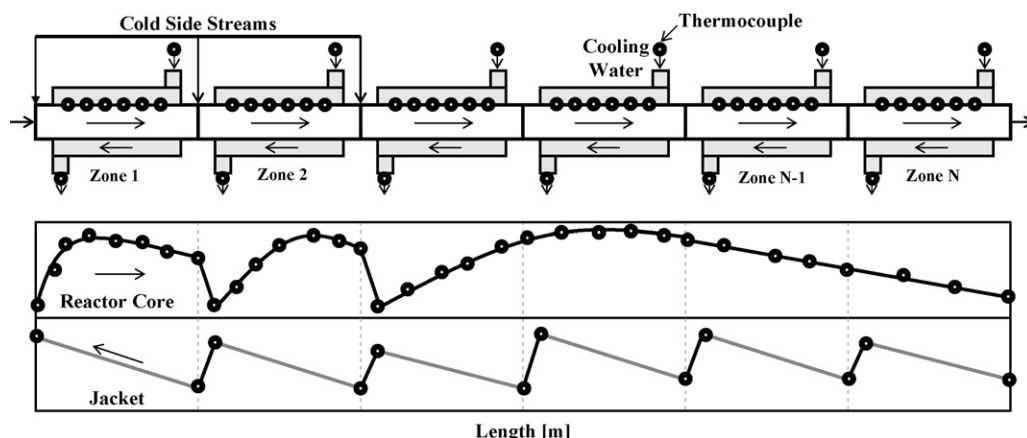 *E-mail address:* vzavala@andrew.cmu.edu (V.M. Zavala).

Fig. 1. Schematic representation of multi-zone LDPE tubular reactor (top). Typical reactor core and jacket temperature profiles (bottom).

design and operating conditions and the resulting polymer properties (Goto et al., 1981; Kim & Iedema, 2004; Luft, Bitsch, & Seidl, 1977). This increased level of understanding has translated into numerous first-principles models of different complexity (Bokis, 2001; Brandolin, Lacunza, Ugrin, & Capiati, 1996; Kiparissides, Verros, & McGregor, 1993; Kiparissides et al., 2005; Zabisky, Chan, Gloor, & Hamielec, 1992). In addition, the recent use of parameter estimation techniques has improved significantly the predictive capabilities of these models (Kiparissides et al., 2005; Zavala & Biegler, 2006). Some of these models have been used for off-line tasks such as reactor design and dynamic transient analysis (Häfele, Kienle, Boll, & Schmidt, 2006; Pertsinidis, Papadopoulos, & Kiparissides, 1996). As a natural step, it is desired to use these models to perform on-line tasks such as real-time optimization and model-based control (Kiparissides, Verros, Pertsinidis, & Goosens, 1996; Zavala & Biegler, 2008). In order to do this, it is necessary to develop an appropriate on-line estimation strategy able to accommodate the rigorous model in on-line industrial environments where limited and noisy measurement information and uncertain time-varying phenomena are usually encountered. In this context, moving horizon estimation (MHE) represents an attractive alternative.

As with any estimation strategy, the objective of MHE is to reconstruct the full state of the process using the available measurement information. The main difference between MHE and recursive estimation techniques such as Extended Kalman Filters and Luenberger observers is that the estimator problem is cast directly as an on-line optimization problem (Rawlings & Bakshi, 2006; Haseltine & Rawlings, 2005). Crucial advantages of this approach are the ability to handle bound constraints to filter out estimation regions with no physical meaning, the ability to handle sophisticated dynamic models in non-standard forms (e.g. boundary conditions on complex domains) and the ability to use computationally efficient numerical optimization algorithms. Despite these advantages, the direct application of MHE to LDPE processes is complicated by the computational complexity of the associated tubular reactor models. For applications of industrial interest, rigorous dynamic models able to capture wide operating regions and strong dynamic transients are required. These models are described by large sets of highly complex partial, differential and algebraic equations (PDAEs) (Häfele et al., 2006).

In this work, we present a large-scale MHE strategy for LDPE tubular reactors. The approach incorporates a detailed first-principles PDAE model. Section 2 presents the model details and Section 3 describes issues related to the incorporation of the model into the MHE formulation. Section 4 describes the computational strategy used to solve the on-line MHE problem. Here, we propose a full discretization strategy of the reactor model based on orthogonal collocation on finite elements and implicit Euler schemes. We will see that this approach results into large-scale and sparse nonlinear programming (NLP) problems that can be solved efficiently with the state-of-the-art interior point solver IPOPT (Wächter & Biegler, 2006). Finally, we describe how to use the capabilities of the IPOPT solver to analyze the convergence properties of the MHE estimator. In Section 5, we analyze the practical performance of the estimator in a typical scenario arising in the operation of industrial LDPE reactors. Here, we demonstrate that the on-line implementation of MHE strategies in LDPE reactors is computationally feasible. The last section concludes the paper and presents directions for future work.

2. Dynamic model of LDPE multi-zone tubular reactor

We consider a general first-principles dynamic model for multi-zone LDPE tubular reactors. The model involves conservation equations describing the evolution of the reacting mixture at supercritical conditions in time and space. In addition, it incorporates detailed energy balances for the reactor core, the reactor wall and the countercurrent jackets. A very large number of complex semi-empirical correlations are used to estimate the thermodynamic and transport properties of the reacting mixture. A detailed free-radical copolymerization mechanism is also incorporated and is presented in Table 1. Here, symbols I_i with $i \in \{1, \ldots, N_I\}$, $R^\cdot$, M_1, M_2 and S_i with $i \in \{1, \ldots, N_S\}$ denote the initiators, radicals, monomer, comonomer and chain-transfer agent (CTA) molecules, respectively. Symbol f_i represents the efficiency of initiator i. Symbols $P_{r,s}$ represent "live" polymer chains ending with a monomer unit; with r monomer units and s comonomer units. Similarly, $Q_{r,s}$ are "live" polymer chains with r, s degrees of polymerization but ending with a comonomer unit and $M_{r,s}$ are "dead" polymer chains. The method of moments is used to track the polymer macromolecular properties (Kiparissides et al., 1996). Empirical correlations are used to compute the end-use polymer properties such as the resin density and melt-index.

The proposed dynamic model is an extension of a previously reported steady-state model used for off-line parameter estimation. Several modifications to the overall energy balances in the reactor were necessary and are described in detail in this section. For a detailed description of the material balances and of the thermodynamic and transport equations, we refer the reader to Zavala and Biegler (2006).

Table 1
Copolymerization kinetic mechanism of LDPE tubular reactor model.

Initiator(s) decomposition	Incorporation of CTAs
$I_i \xrightarrow{f_i k_{d_i}} 2R$ $i = 1, N_I$	$P_{r,s} + S_i \xrightarrow{k_{spi1}} P_{r+1,s}$ $i = 1, N_s$
Chain initiation	$Q_{r,s} + S_i \xrightarrow{k_{spi2}} Q_{r,s+1}$ $i = 1, N_s$
$R^{\cdot} + M_1 \xrightarrow{k_{I_1}} P_{1,0}$	Termination by combination
$R^{\cdot} + M_2 \xrightarrow{k_{I_2}} Q_{0,1}$	$P_{r,s} + P_{x,y} \xrightarrow{k_{tc11}} M_{r+x,s+y}$
Chain propagation	$P_{r,s} + Q_{x,y} \xrightarrow{k_{tc12}} M_{r+x,s+y}$
$P_{r,s} + M_1 \xrightarrow{k_{p11}} P_{r+1,s}$	$Q_{r,s} + Q_{x,y} \xrightarrow{k_{tc22}} M_{r+x,s+y}$
$P_{r,s} + M_2 \xrightarrow{k_{p12}} Q_{r,s+1}$	Termination by disproportionation
$Q_{r,s} + M_1 \xrightarrow{k_{p21}} P_{r+1,s}$	$P_{r,s} + P_{x,y} \xrightarrow{k_{td11}} M_{r,s} + M_{x,y}$
$Q_{r,s} + M_2 \xrightarrow{k_{p22}} Q_{r,s+1}$	$P_{r,s} + Q_{x,y} \xrightarrow{k_{td12}} M_{r,s} + M_{x,y}$
Chain transfer to monomer	$Q_{r,s} + Q_{x,y} \xrightarrow{k_{td22}} M_{r,s} + M_{x,y}$
$P_{r,s} + M_1 \xrightarrow{k_{fm11}} P_{1,0} + M_{r,s}$	Backbiting
$P_{r,s} + M_2 \xrightarrow{k_{fm12}} Q_{0,1} + M_{r,s}$	$P_{r,s} \xrightarrow{k_{b1}} P_{r,s} or Q_{r,s}$
$Q_{r,s} + M_1 \xrightarrow{k_{fm21}} P_{1,0} + M_{r,s}$	$P_{r,s} \xrightarrow{k_{b2}} Q_{r,s} or P_{r,s}$
$Q_{r,s} + M_2 \xrightarrow{k_{fm22}} Q_{0,1} + M_{r,s}$	β-scission of sec- and tert-radicals
Chain transfer to polymer	$P_{r,s} \xrightarrow{k_{\beta1}} M^{=}_{r,s} + P_{1,0}$
$P_{r,s} + M_{x,y} \xrightarrow{k_{fp11}} P_{x,y} + M_{r,s}$	$P_{r,s} \xrightarrow{k_{\beta2}} M^{=}_{r,s} + Q_{0,1}$
$P_{r,s} + M_{x,y} \xrightarrow{k_{fp12}} Q_{x,y} + M_{r,s}$	$P_{r,s} \xrightarrow{k'_{\beta1}} M^{=}_{r,s} + P_{1,0}$
$Q_{r,s} + M_{x,y} \xrightarrow{k_{fp21}} P_{x,y} + M_{r,s}$	$P_{r,s} \xrightarrow{k'_{\beta2}} M^{=}_{r,s} + Q_{0,1}$
$Q_{r,s} + M_{x,y} \xrightarrow{k_{fp22}} Q_{x,y} + M_{r,s}$	
Chain transfer to CTAs	
$P_{r,s} + S_i \xrightarrow{k_{si1}} P_{1,0} + M_{r,s}$ $i = 1, N_s$	
$Q_{r,s} + S_i \xrightarrow{k_{si2}} Q_{0,1} + M_{r,s}$ $i = 1, N_s$	

2.1. Dynamic energy balances

We make use of Fig. 2 to illustrate the different components of the dynamic energy balance equations. The dynamic responses of the reacting mixture flowing inside the reactor are *fast* due to the extremely high velocities encountered (Kiparissides et al., 1993). Consequently, it is safe to assume that the reacting mixture is at a quasi-steady-state at all times. Accordingly, the evolution of reactor core temperature can be described by the following ordinary differential equation,

$$\rho_k(t,x) c_{p_k}(t,x) v_k(t,x) \frac{\partial T_k}{\partial x}$$
$$= \frac{\pi d^{in} \mathbf{U}_k^{in}(t)}{A_k}(T_k^W(t,x) - T_k(t,x)) - \Delta H_R(t,x) \tag{1a}$$

$$T_k(t,0) = T_k^{inlet}(t) \tag{1b}$$

The axial dimension along each one of the zones is denoted by $x \in [0, x_k^L]$ where x_k^L is the total length of a particular zone k. The time dimension is denoted by symbol t. The above system of equations is defined for all the reactor zones $k = 1, \ldots, N_Z$. The reacting mixture temperature at a particular zone is denoted by
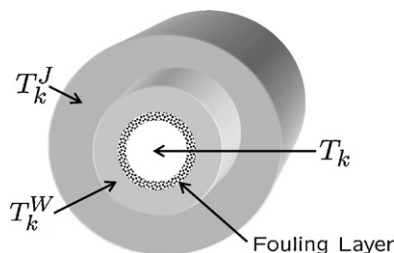

Fig. 2. Schematic representation of reactor-wall-jacket interface.

T_k and the wall temperature is represented by T_k^W. The mixture density, heat capacity and velocity, are represented by ρ_k, c_{p_k} and v_k, respectively. The overall heat of polymerization generated by chain propagation is represented by term ΔH_R. The overall heat transfer coefficient at the core-wall interface is represented by $\mathbf{U}_k^{in}$, A_k denotes the inner cross-sectional area and d^{in} is the inner diameter. The time-varying inlet temperature at a particular zone $T_k^{inlet}(t)$ is computed through boundary conditions consisting of energy balances at the feed points.

The reacting mixture is cooled down through a jacket cooling system. Due to the extremely high operating pressures, a thick stainless steel wall exists at the interface. This results in a large thermal capacitance that make the dynamic responses of the wall quite slow (order of minutes). In addition, due to the large thickness, there exists a temperature gradient across the radial position of the wall. A rigorous way to account for this would be to incorporate a two-dimensional energy balance along the axial and radial positions. However, this approach would result in a three-dimensional PDE defined at each zone, which would increase significantly the complexity of the reactor model. In order to avoid this, we follow the approach of Häfele et al. (2006). Here, we assume that the entire radial profile can be lumped into an average radial wall temperature. Accordingly, the wall temperature profile along the axial and time dimensions can be described by a parabolic PDE of the form,

$$\rho_k^W(t,x) c_{p,k}^W(t,x) \frac{\partial T_k^W}{\partial t} - \lambda_k^W(t,x) \frac{\partial^2 T_k^W}{\partial x^2}$$
$$= \frac{\pi d^{in} \mathbf{U}_k^{in}(t)}{A_k^W}(T_k(t,x) - T_k^W(t,x)) - \frac{\pi d^{out} \mathbf{U}_k^{out}(t)}{A_k^W}(T_k^W(t,x) - T_k^J(t,x)) \tag{2a}$$

$$T_k^W(0,x) = T_k^{W,0}(x) \tag{2b}$$

$$-A_k^W \lambda_k^W(t,x) \frac{\partial T_k^W}{\partial x}(t,0) = \dot{\mathbf{Q}}_k^{in} \tag{2c}$$

$$-A_k^W \lambda_k^W(t,x) \frac{\partial T_k^W}{\partial x}(t,x_k^L) = \dot{\mathbf{Q}}_k^{out} \tag{2d}$$

where T_k^J denotes the temperature of the cooling water flowing along the jacket at a particular zone k and $T_k^{W,0}(x)$ are the initial conditions of the wall temperature profile. Symbols ρ_k^W, $c_{p,k}^W$ and λ_k^W denote the density, heat capacity and thermal conductivity of the stainless steel wall, respectively. The overall heat transfer coefficient at the interface between the wall and the jacket is denoted by $\mathbf{U}_k^{out}$, A_k^W is the cross-sectional area of the wall and the outer diameter is d^{out}. The axial inlet and outlet heat conduction flows across the wall are denoted by $\dot{\mathbf{Q}}_k^{in}$ and $\dot{\mathbf{Q}}_k^{out}$, respectively. It is important to note that there exists heat flow continuity at the zone boundaries. Therefore, $\dot{\mathbf{Q}}_k^{in} = \dot{\mathbf{Q}}_{k-1}^{out}$, $k = 2, \ldots, N - 1$. At the reactor extremes, the heat flows $\dot{\mathbf{Q}}_0^{in}$ and $\dot{\mathbf{Q}}_N^{out}$ can be calculated through natural convection expressions or can be assumed to be zero for a sufficiently long pipe.

Each reactor zone is equipped with an independent jacket cooling system where cooling water flows countercurrently to the reacting mixture inside the pipe. We assume plug flow in the jacket and negligible heat losses to the environment (perfect insulation). Accordingly, the dynamic evolution of the cooling water temperature at each zone can be described by the following first-order PDE,

$$\rho_k^J(t,x) c_{p,k}^J(t,x) \left(\frac{\partial T_k^J}{\partial t} - v_k^J(t,x) \frac{\partial T_k^J}{\partial x} \right)$$
$$= \frac{\pi d^{out} \mathbf{U}_k^{out}(t)}{A_k^J}(T_k^W(t,x) - T_k^J(t,x)) \tag{3a}$$

$$T_k^J(t, x_k^L) = T_k^{J,\text{inlet}}(t) \tag{3b}$$

$$T_k^J(0, x) = T_k^{J,0}(x) \tag{3c}$$

where ρ_k^J, $c_{p,k}^J$ and ν_k^J are the density, heat capacity and velocity of the cooling water. The cross-sectional area of the jacket annulus is denoted by A_k^J. The time-varying inlet temperature of the cooling water is denoted by $T_k^{J,\text{inlet}}(t)$ and the initial conditions for jacket temperature profile are given by $T_k^{J,0}(x)$.

2.2. Dynamic model representation

To represent the overall dynamic model in simple terms, we collapse the PDAEs corresponding to material and energy balances, thermodynamics and transport expressions and kinetic expressions for all zones into a single set of PDAEs. This can be done by grouping the states corresponding to all zones into a single variable vector and defining the continuity equations between zones as algebraic equations. Following this reasoning, we represent the multi-zone reactor model as,

$$\frac{\partial z}{\partial t} + \nu(t, x)\frac{\partial z}{\partial x} + \lambda(t, x)\frac{\partial^2 z}{\partial x^2} = f_z(z(t,x), w(t,x), y(t,x), p(t), u(t)) \tag{4a}$$

$$\frac{\partial w}{\partial x} = f_w(z(t,x), w(t,x), y(t,x), p(t), u(t)) \tag{4b}$$

$$0 = f_y(z(t,x), w(t,x), y(t,x), p(t), u(t)) \tag{4c}$$

$$\chi(t, x) = h(z(t,x), w(t,x), y(t,x), p(t), u(t)) \tag{4d}$$

$$z(0, x) = z^0(x) \tag{4e}$$

where $z(t, x) \in \Re^{n_z}$ represents the differential states in space and time with initial conditions $z^0(x)$. These states correspond to the cooling water temperature and the reactor wall temperature at all zones. Symbol $w(t, x) \in \Re^{n_w}$ denotes differential states in space such as the reacting mixture temperature, the molar flow rates of gaseous components and the chain moments, among others. Symbol $y(t, x) \in \Re^{n_y}$ denotes the algebraic states corresponding to the rest of the model variables such as the cooling water and reacting mixture velocities, densities, heat capacities, among others. Symbol $p(t)$ denotes time-varying parameters used to account for unmodeled effects and uncertainty. Symbol $u(t)$ denotes the zone inputs corresponding to side-stream inlet temperatures and flow rates, among others. In the actual reactor, the inputs can only be fed at the beginning and end of each reactor zone, so there is no explicit dependence on the internal spatial dimension x. For convenience, we also define a set of variables $\chi(t, x) \in \Re^{n_\chi}$ to map the model states and inputs into the measured variables in the actual LDPE process. The number of actual equations depends on the number of gaseous components present in the reacting mixture during the production of a particular grade. On average, the model will contain 3 PDEs, 20 ODEs and 500 AEs defined at each reactor zone.

The boundary conditions of system (4) can be expressed in the general form,

$$0 = \varphi\left(z(t, 0), z(t, x^L), \frac{\partial z}{\partial x}(t, 0), \frac{\partial z}{\partial x}(t, x^L), w(t, 0), u(t)\right). \tag{5}$$

3. Moving horizon estimation

Since any mathematical abstraction of a real process is never complete due to uncertain phenomena or unmeasured distur-

bances, it is often necessary to use a filter or estimator to make the model useful in on-line environments. In this section, we present the formulation of a MHE estimator for LDPE tubular reactor processes.

3.1. Time-varying uncertainty and measurements

In LDPE processes, there exist multiple sources of uncertainty that are difficult to capture through the rigorous model. One of the most important issues encountered is the persistent deposition of polymer on the internal walls along the reactor (Lacunza et al., 1998). This fouling layer has poor conduction properties and tends to dominate the overall heat transfer rate between the reactor core and the walls. It has been observed that the fouling resistance can account for more than 80% of the overall heat transfer resistance (Bokis, 2001). The deposition rate and distribution of polymer depends on multiple factors which are difficult to explain from a mechanistic point of view. On the other hand, the availability of a first-principles model allows to map the sources of uncertainty to physical parameters that can be estimated on-line. In this work, we track the fouling deposition in time through the estimation of the internal heat transfer coefficients along each zone $\mathbf{U}_k^{\text{in}}(t)$. Another important source of uncertainty is the continuous decay of the initiator efficiency due to caging effects and undesired reactions with impurities (Luft et al., 1977). This uncertainty can be tracked by estimating the efficiencies of all initiators in the reactor (Kiparissides et al., 1996). While the proposed estimation strategy is general and can handle decaying initiator efficiencies, we focus our attention to the fouling problem.

A second issue arising in industrial LDPE units is that there exists limited measurement information to infer the internal reactor phenomena. LDPE reactors are usually monitored and controlled using distributed measurements of the reactor core temperature. A typical industrial reactor can easily contain around a hundred thermocouples. Measurements of the inlet and outlet temperatures of the cooling water and the overall reactor conversion are also available. In some cases, it is also possible to obtain continuous measurements of the polymer melt index. As part of input measurements, we include with the initiator, monomer and chain-transfer agent side stream flow rates and temperatures as well as the inlet pressure of the reactor. The compositions of the side steams entering the reactor are calculated through material balances.

3.2. MHE problem formulation

Imagine that the LDPE process is currently located at sampling time t_j and we have a *past* input and output measurement history $\{\eta_j, \eta_{j-1}, \ldots, \eta_{j-N}\}$ distributed over a time horizon containing N sampling times of equal length $\delta = t_j - t_{j-1}$. Using this information, we seek to *infer* the current state of the reactor $z(t_j, x), w(t_j, x), y(t_j, x)$, the parameters $p(t_j)$ and, if needed, the reconciled inputs $u(t)$ through the rigorous model. We assume that the model structure is correct and that all the uncertainty related to the real process can be encapsulated in the model parameters $p(t)$, in the initial conditions $z^0(x)$ and in the measurement errors. Following this reasoning, an estimate of the current state of the process can be computed through the solution of a least-squares dynamic optimization problem of the form,

$$\min_{p(t), z^0(x), u(t)} \quad (z^0(x) - \bar{z}^0(x))^\mathrm{T} \mathbf{\Pi}_0^{-1}(z^0(x) - \bar{z}^0(x))$$
$$+ \sum_{j=1}^{N} \sum_{i=1}^{N_m} (\eta_{j-N}^{(i)} - \chi(j\delta, x_i))^\mathrm{T} \mathbf{R}^{-1}(\eta_{j-N}^{(i)} - \chi(j\delta, x_i)) \tag{6a}$$

$$\overset{\text{s.t.}}{\frac{\partial z}{\partial t}} + \nu(t,x)\frac{\partial z}{\partial x} + \lambda(t,x)\frac{\partial^2 z}{\partial x^2} = f_z(z(t,x), w(t,x), y(t,x), p(t), u(t))$$

$$(6b)$$

$$\frac{\partial w}{\partial x} = f_w(z(t,x), w(t,x), y(t,x), p(t), u(t)) \tag{6c}$$

$$0 = f_y(z(t,x), w(t,x), y(t,x), p(t), u(t)) \tag{6d}$$

$$\chi(t,x) = h(z(t,x), w(t,x), y(t,x), p(t), u(t)) \tag{6e}$$

$$0 \geq g(z(t,x), w(t,x), y(t,x), p(t), u(t)) \tag{6f}$$

$$z(0,x) = z^0(x) \tag{6g}$$

$$0 = \varphi\left(z(t,0), z(t,x^L), \frac{\partial z}{\partial x}(t,0), \frac{\partial z}{\partial x}(t,x^L), w(t,0), u(t)\right)$$

$$t \in [0\,N\delta]. \tag{6h}$$

Note that the process measurements are only defined at discrete points in time $j\delta$, with sampling interval δ, and space x_i. Symbol $\eta_j^{(i)}$ denotes the i th spatial measurement in vector η_j. The measurement vector contains both output and input measurements with covariance $\mathbf{R} \in \Re^{n_\chi \times n_\chi}$. The total number of measurements in space is denoted by N_m. The MHE problem contains a large number of degrees of freedom including the parameters, the initial conditions for the dynamic states and the inputs. Variable $\bar{z}^0(x)$ denotes the *a priori* value of the initial state with covariance $\mathbf{\Pi}_0 \in \Re^{n_z \times n_z}$. The first term in the objective function is the *arrival cost*, which summarizes past measurement information before sampling time t_{j-N}.

From the solution of the optimization problem, we extract the estimate of the current state of the process as $z(t_j,x) \leftarrow z^*(\delta N, x), w(t_j,x) \leftarrow w^*(\delta N, x), y(t_j,x) \leftarrow y^*(\delta N, x)$, the current parameters $p(t_j) \leftarrow p^*(\delta N)$ and the reconciled inputs $u(t_j)$. At the next sampling time t_{j+1}, we avoid adding extra measurements into an infinitely long estimation horizon by dropping the last measurement and incorporating the new one to obtain the new measurement history $\{\eta_{j+1}, \eta_j, \ldots, \eta_{j+1-N}\}$. Accordingly, we update the *a priori* estimate of the initial state using the previous solution as $\bar{z}^0(x) \leftarrow z^*(\delta, x)$. In some cases it is also necessary to update the covariance matrix $\mathbf{\Pi}_0$ using the covariance of the predicted state $z^*(\delta, x)$ in order to summarize past measurement information and to ensure stability and convergence of the estimator (Rawlings & Bakshi, 2006). However, this update might not be required if the system satisfies strong observability conditions (Alessandri, Baglietto, & Battistelli, 2008).

Note that the MHE formulation considered in this work assumes a perfect model of the plant. Structural model mismatch can be considered by extending the formulation with appropriate disturbance models. A serious limitation that is normally attributed to MHE is that it requires on-line solutions of large-scale optimization problems. Since this is a time-critical application, the optimization problem needs to be solved as quickly as possible. In the following section, we propose a solution strategy that allows to solve the on-line MHE problem in a reasonable amount of time.

4. Solution strategy

We propose a full discretization approach to solve the infinite-dimensional MHE problem (6). This approach enjoys a favorable computational complexity and allows to handle the complex boundary conditions encountered across the reactor (Biegler, Cervantes, & Wächter, 2002). Upon full discretization, the MHE problem is cast as a general NLP problem in purely algebraic form. In this section, we discuss the different components of this solution strategy.
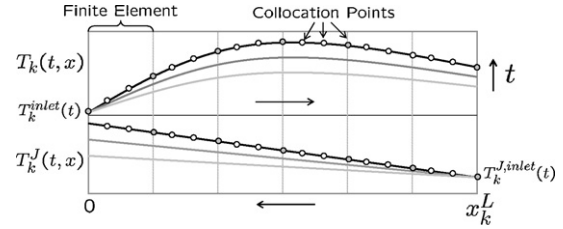

Fig. 3. Schematic representation of discretization approach. Reactor core (top) and Jacket (bottom).

4.1. Discretization

As can be seen in Fig. 1, LDPE reactor models present steep temperature profiles in space. In addition, the model presents steep profiles for some gaseous components such as the initiators that are totally consumed immediately after they are injected into the reaction zones. On the other hand, the quasi-steady-state assumption for the reactor core eliminates stiffness problems along the time dimension. Motivated by these observations, we use a fine discretization mesh in space and a coarse mesh in time. We follow a finite element discretization approach at Radau collocation points in the space dimension (Biegler et al., 2002). An advantage that Radau collocation provides is that the last collocation point matches the terminal spatial coordinate. This allows to impose the multi-point boundary conditions across the reactor zones in a straightforward manner. In Fig. 3, we present a conceptual representation of the discretization approach for the reactor and jacket temperature profiles of a particular zone.

For the actual implementation, we use an average of 10 finite elements for the reaction zones and 2 finite elements for the cooling zones. Three collocation points are used. Upon spatial discretization, the PDAE reactor model translates into a DAE model containing around 9000–10,000 DAEs in time. For time discretization, we use an implicit Euler (1 pt. Radau) scheme and place the discretization points at the sampling times. An average of 5 points are used. With this, the DAE model is converted into an algebraic model with around 40,000–50,000 equations. The algebraic model is very sparse. On average, the Jacobian contains around 10 non-zero entries per row. That is, only 10 variables out of 40,000–50,000 appear in each equation on average.

4.2. Interior-point NLP solver

The discretized MHE problem presents a natural forward structure in time that could be exploited with tailored strategies such as Riccati-like recursions (Zavala, Laird, & Biegler, 2008). However, the computational complexity of this approach will not be favored due to the large number of dynamic states resulting from the spatial discretization. In addition, due to the high nonlinearity and ill-conditioning of the LDPE model, a more general NLP solver equipped with the required numerical capabilities is preferred. Because of these reasons, we solve the MHE problem as a general NLP problem of the form,

$$\min_{\mathbf{x}} f(\mathbf{x}) \tag{7a}$$

$$\text{s.t.} \quad c(\mathbf{x}) = 0 \tag{7b}$$

$$\mathbf{x} \geq 0. \tag{7c}$$

where variable $\mathbf{x} \in \Re^{n_\mathbf{x}}$ contains all the discretized variables of the MHE problem.

Full-space interior-point solvers have become a popular choice for the solution of large-scale and sparse NLPs as those arising in this application. There exist several solvers available such as

LOQO, KNITRO and IPOPT (Benson, Shanno, & Vanderbei, 2002; Byrd, Gilbert, & Nocedal, 2000; Wächter & Biegler, 2006). In this work, we use the open-source solve IPOPT to implement our developments.

As with any interior-point solver, IPOPT handles the inequality constraints of problem (7) implicitly by adding barrier terms to the objective function,

$$\min_{\mathbf{x}} f(\mathbf{x}) + \mu \sum_{i=1}^{n_{\mathbf{x}}} \ln(\mathbf{x}^{(i)}) \tag{8a}$$

$$\text{s.t.} \quad c(\mathbf{x}) = 0 \tag{8b}$$

where $\mathbf{x}^{(i)}$ denotes the i th component of vector $\mathbf{x}$. Solving (8) for a decaying sequence of $\mu \to 0$ results in an efficient strategy to solve the original NLP (7). At a particular value of μ, IPOPT tries to solve the Karush-Kuhn-Tucker (KKT) conditions of the barrier problem (8),

$$\nabla_{\mathbf{x}} f(\mathbf{x}) + \nabla_{\mathbf{x}} c(\mathbf{x}) \lambda - \nu = 0 \tag{9a}$$

$$c(\mathbf{x}) = 0 \tag{9b}$$

$$\mathbf{X} \cdot \mathbf{V} e = \mu e \tag{9c}$$

where $\mathbf{X} = \text{diag}(\mathbf{x})$, $\mathbf{V} = \text{diag}(\nu)$ and $e \in \Re^{n_{\mathbf{x}}}$ is a vector of ones. Symbols $\lambda \in \Re^{\lambda}$ and $\nu \in \Re^{n_{\mathbf{x}}}$ are Lagrange multipliers for the equality constraints and bounds, respectively. The gradient of the objective function is $\nabla_{\mathbf{x}} f(\mathbf{x}) \in \Re^{n_{\mathbf{x}}}$ while $\nabla_{\mathbf{x}} c(\mathbf{x}) \in \Re^{n_{\mathbf{x}} \times n_{\lambda}}$ is the constraint Jacobian. To solve this system of nonlinear equations, IPOPT applies Newton's method. At each iteration i, the search direction for the primal $\mathbf{x}$ and dual λ, ν variables is computed by linearization of the KKT conditions (9),

$$\begin{bmatrix} \mathbf{H}_i & \mathbf{A}_i & -\mathbb{I}_{n_{\mathbf{x}}} \\ \mathbf{A}_i^{\mathsf{T}} & 0 & 0 \\ \mathbf{V}_i & 0 & \mathbf{X}_i \end{bmatrix} \begin{bmatrix} \Delta \mathbf{x}_i \\ \Delta \lambda_i \\ \Delta \nu_i \end{bmatrix} = - \begin{bmatrix} \nabla_{\mathbf{x}} f(\mathbf{x}_i) + \mathbf{A}_i \lambda_i - \nu_i \\ c(\mathbf{x}_i) \\ \mathbf{X}_i \mathbf{V}_i e - \mu e \end{bmatrix} \tag{10}$$

where $\mathbf{A}_i := \nabla_{\mathbf{x}} c(\mathbf{x}_i)$. Matrix $\mathbf{H}_i \in \Re^{n_{\mathbf{x}} \times n_{\mathbf{x}}}$ is the Hessian of the Lagrange function $\mathcal{L} = f(\mathbf{x}_i) + c(\mathbf{x}_i)^T \lambda_i - \nu_i^T \mathbf{x}_i$ evaluated at the current iteration and $\mathbb{I}_{n_{\mathbf{x}}}$ is the identity matrix. We provide exact Hessian and Jacobian information to IPOPT through the modeling platform AMPL (Fourer, Gay, & Kernighan, 1992). With this, we guarantee fast local convergence of Newton's method and we are able to handle problems with many degrees of freedom without altering these local convergence properties.

Computing the search direction from (10) is the most expensive step in the algorithm since it involves the factorization of the KKT matrix on the right-hand side. Note that the KKT matrix implicity incorporates the Jacobian of the large-scale discretized PDAE model which is very sparse. In order to solve this linear system, we follow a direct sparse factorization approach. With this, we exploit only the *sparsity pattern* of the KKT matrix. The computational complexity of this strategy is in general very favorable, scaling nearly linearly and at most quadratically with the overall dimensions of the NLP (e.g. length of estimation horizon, number of states and number of degrees of freedom). In the context of large-scale state estimation, this favorable complexity makes MHE more attractive than traditional Kalman-like estimators (Zavala, Laird, & Biegler, 2007). On the other hand, significant fill-in and computer memory bottlenecks might arise during the direct factorization strategy if the sparsity pattern is not properly exploited. In order to factorize the KKT matrix, we use the linear solver MA57 from the Harwell library (Duff, 2004). Since the structure of the KKT matrix does not change between iterations, the linear solver needs to analyze the sparsity pattern *only once*. During this analysis phase,

the linear solver permutes the matrix to reduce fill-in and computer memory requirements in the factorization phase. Different reordering strategies can be used in MA57. The default strategy is an approximate minimum degree (AMD) ordering algorithm. Another strategy is a nested dissection (ND) algorithm based on the multi-level graph partitioning strategy, implemented in Metis (Karypis & Kumar, 1999). For very large problems such as those arising from PDE-constrained optimization, nested dissection excels at identifying high-level (coarse-grained) structures and thus plays a crucial role in the factorization time and reliability of the linear solver.

IPOPT also applies a regularization scheme of the Hessian matrix to account for directions of negative curvature which are commonly encountered in ill-posed and/or highly nonlinear NLPs. From a practical point of view, it is particularly useful to monitor the regularization term of the Hessian matrix. If this regularization term is zero at the solution, we can guarantee that the optimal point is a well-defined minimum satisfying strong second order conditions (Nocedal & Wright, 1999). In other words, the reduced Hessian (Hessian projected into the null-space of the Jacobian of the active constraints) is positive definite. In the context of estimation problems, this implies that the measurements are informative enough to infer or observe the degrees of freedom (e.g. parameters, initial conditions, inputs) (Bard, 1974).

4.2.1. Covariance information extraction

In MHE problems, we are also interested in *quantifying* the observability of the estimated states and parameters. This can be done by analyzing the principal components of the reduced Hessian matrix at the solution of the problem. In order to extract reduced Hessian information from IPOPT, we make use of a recently implemented capability for *post-optimal* analysis. The main idea is to reconstruct the reduced Hessian using backsolves with the KKT matrix evaluated at the solution (Zavala et al., 2008). To explain the mechanics of this, we split the variable vector as $\mathbf{x}^{\mathsf{T}} = [\bar{\mathbf{x}}^{\mathsf{T}} \hat{\mathbf{x}}^{\mathsf{T}}]$ where $\bar{\mathbf{x}}$ is a vector of dependent variables and $\hat{\mathbf{x}}$ is a vector of independent variables of the same dimension as the number of degrees of freedom of the NLP. According to this variable partition, the Jacobian can be rearranged as $\mathbf{A}^{\mathsf{T}} = [\mathbf{A}_*^{\bar{\mathbf{x}}^{\mathsf{T}}} | \mathbf{A}_*^{\hat{\mathbf{x}}^{\mathsf{T}}}]$ where $\mathbf{A}_*^{\bar{\mathbf{x}}}$ is a nonsingular square matrix. Following this reasoning, we can represent the KKT system (10) evaluated at the solution as,

$$\begin{bmatrix} \mathbf{H}_*^{\bar{\mathbf{x}}\bar{\mathbf{x}}} & \mathbf{H}_*^{\bar{\mathbf{x}}\hat{\mathbf{x}}} & \mathbf{A}_*^{\bar{\mathbf{x}}} \\ \mathbf{H}_*^{\hat{\mathbf{x}}\bar{\mathbf{x}}} & \mathbf{H}_*^{\hat{\mathbf{x}}\hat{\mathbf{x}}} & \mathbf{A}_*^{\hat{\mathbf{x}}} \\ \mathbf{A}_*^{\bar{\mathbf{x}}^{\mathsf{T}}} & \mathbf{A}_*^{\hat{\mathbf{x}}^{\mathsf{T}}} & 0 \end{bmatrix} \begin{bmatrix} \Delta \bar{\mathbf{x}} \\ \Delta \hat{\mathbf{x}} \\ \Delta \lambda \end{bmatrix} = - \begin{bmatrix} r_{\bar{\mathbf{x}}} \\ r_{\hat{\mathbf{x}}} \\ r_{\lambda} \end{bmatrix} . \tag{11}$$

Here, notice that we have eliminated the terms corresponding to variable bounds in order to simplify the presentation. In addition, note that the right hand sides are zero at the solution of the NLP. It is possible to prove that, if we set $r_{\bar{\mathbf{x}}} = r_{\lambda} = 0$ and $r_{\hat{\mathbf{x}}}$ to the j th column of the identify matrix $\mathbb{I}_{n_{\hat{\mathbf{x}}}}(:,j)$ then, the search step $\Delta \hat{\mathbf{x}}$ becomes the j th column of the inverse of the reduced Hessian matrix. In other words,

$$\Delta \hat{\mathbf{x}} = (\mathbf{Z}^{\mathsf{T}} \mathbf{H}_* \mathbf{Z})^{-1} (:,j) \tag{12}$$

where $\mathbf{Z}$ is a null-space matrix of the full Jacobian $\mathbf{A}_*$ with structure,

$$\mathbf{Z} = \begin{bmatrix} -\mathbf{A}_*^{\bar{\mathbf{x}}^{-1}} \mathbf{A}_*^{\hat{\mathbf{x}}} \\ \mathbb{I}_{\hat{\mathbf{x}}} \end{bmatrix} . \tag{13}$$

Using this property, we can extract reduced Hessian information from the full-space NLP solver inexpensively through backsolves with the already factorized KKT matrix. It is also possible to prove that, if we place the identity matrix $\mathbb{I}_{n_{\hat{\mathbf{x}}}}$ on the rows corresponding
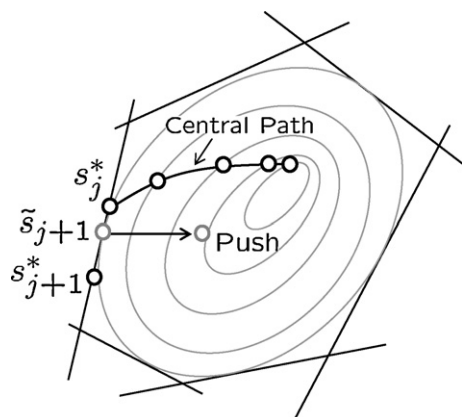
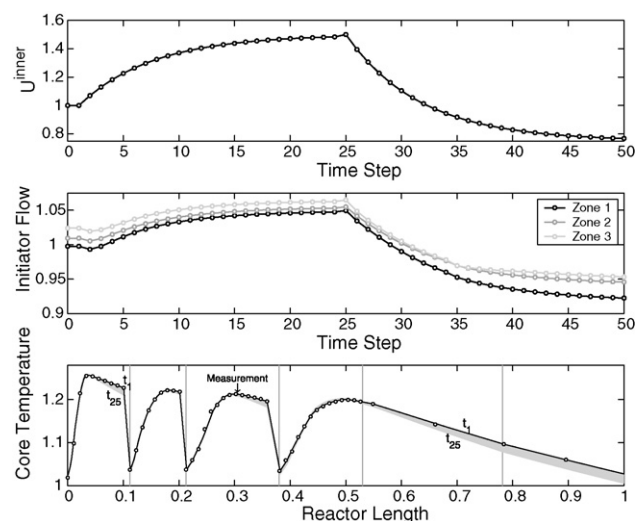Fig. 4. Schematic representation of warm-starting strategy.

Fig. 5. Description of case study. Defouling–fouling cycle for inner heat transfer coefficient of Zone 1 (top). Closed-loop response of initiator flow rate of Zone 1 (middle). Dynamic response of reactor core temperature profile (bottom).

to the state $z^*(\delta N, x)$ from MHE problem (6a), the resulting matrix becomes the covariance of the current state estimates $\mathbf{\Pi}_N$ (Zavala et al., in press).

4.2.2. Warm-starting strategy

Moving horizon problems have the important property that subsequent problems are closely related to each other. This fact can be used to find good starting points or *warm-starts* to the current MHE problem (Zavala et al., 2007). A well-known strategy is to shift the optimal values of the states and KKT multipliers forward in time. When the model predictions are accurate and process disturbances are moderate, this strategy can significantly reduce the number of iterations (Diehl, Bock, & Schlöder, 2005; Zavala et al., 2008). While warm-starting strategies work well in active-set solvers, in interior-point solvers it is necessary to modify some of the default algorithmic options to take advantage of this. To explain these concepts, we consider the scenario sketched in Fig. 4. Consider the solution of the current MHE problem s_j^* at time t_j obtained from solving a sequence of barrier problems (8) that form the so-called *central path*. From the solution, we also know which subset of the primal variables is at the bounds (active-set).

In order to warm-start the next problem at t_{j+1}, we shift the variables and KKT multipliers forward in time to generate the warm-start point $\tilde{s}_{j+1}$. Variable shifting is important in order to have a good estimate of the right active-set. In interior-point solvers, we search for the optimal active-set by moving from the interior of the feasible region towards the boundary. Because of this, interior-point solvers push the warm-start point sufficiently inside the feasible region. As a consequence, even if we have with a good warm-starting point with the correct active-set, the interior-point solver will take several iterations to converge to the new solution s_{j+1}^*. This inconsistency can be avoided by setting the barrier parameter μ to a small value and making sure that the solver does not push the warm-start point.

5. Industrial case study

In this section, we analyze the performance of the MHE estimator in typical scenarios arising in industrial LDPE reactors. In particular, we analyze the convergence properties of the MHE estimator in the presence of poor initial guesses of the states and in the face of measurement noise on both inputs and outputs. Finally, we discuss the computational performance of the strategy.

5.1. Estimator performance

LDPE tubular reactors undergo periods where the polymer layer is defouled by means of pressure or thermal shocks (Buchelli et al., 2005a). Since this results in a fluctuating heat transfer capacity of the reactor wall, the control system needs to adjust the multiple reactor inputs (e.g. inlet temperatures, initiators) to keep the reactor temperature profile at target. In this work, we simulate this closed-loop behavior during two transients of the heat transfer coefficients to generate measurement information and to obtain the *true* reference state of the reactor. We use real industrial values of the reactor inputs and outputs obtained from a previous parameter estimation study (Zavala & Biegler, 2006). Consequently, we scale the values of all variables.

The base case study is presented in Figs. 5 and 6. To simulate the cleaning-fouling cycle, we ramp the heat transfer coefficients for all the reactor zones from their nominal value to + 50% at time step 25 and then −20% at time step 50. Each time interval δ corresponds to 5 min of operation. We use an estimation horizon of 5 time steps. In the top graph of Fig. 5, we present the resulting profile for the heat transfer coefficient of Zone 1. In the middle graph, we see that the closed-loop initiator flow rate of Zone 1 drops during the first transition and then increases during the second transition. This is done in order to decrease the reactor conversion and keep the temperature profile as close as possible to the reference profile.
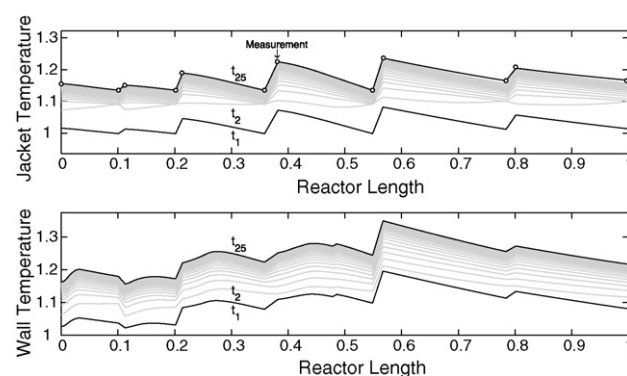

Fig. 6. Description of case study. Dynamic response of jacket temperature profile (top). Dynamic response of wall temperature profile (bottom).

In the bottom graph, we see that the temperature profile does not move significantly from its reference value. The most significant effects can be appreciated at the end of the first four zones (reaction) and in the last two zones (cooling). In the same graph, we also indicate the zones boundaries and the specific location of the thermocouples measuring the reactor core temperature. Note that there exist zones (e.g. beginning of Zone 1) where we have only a few measurements available to shape the temperature profile.

While the reactor temperature profile does not change significantly during the fouling cycle, in the top graph of Fig. 6 we can see that the jacket temperature profile increases significantly during the first transition. In other words, as the heat transfer coefficients increase in time (fouling layer disappears), the cooling water is able to remove more heat from the reactor core and this translates in increasing temperature levels on the jacket side. In addition, note that we only have measurements at the beginning and end of each jacket to help us shape the jacket temperature profile. Finally, note that the dynamic responses of the jackets are fast. At the second time step (t_2), the jacket profile is already far away from the original profile (t_1). This is in sharp contrast with the dynamic response of the wall temperature profile presented in the bottom graph of Fig. 6 where we can appreciate a smoother transition in time.

5.1.1. Nominal case

The simulation results provide the dynamic profiles for all the inputs distributed across the reactor and corresponding states that we use as the *true* states to test the estimator. To analyze the nominal performance of the estimator, we consider the case with the wrong *a priori* guess of the wall and jacket profiles and heat transfer coefficients at time t_0. In addition, we assume that no measurement noise is present. We use the initial guess and the available measurement information to reconstruct the dynamic profiles for the heat transfer coefficients and all the state profiles of the process. We consider two scenarios. In scenario 1, we generate the initial guess for the wall and jacket temperature profiles by perturbing the *true* profiles by −10%. In absolute values, this corresponds to a perturbation of approximately −20 °C to a reference value of 40 °C (i.e.; our guess of the profile is underestimated by 20 °C). In scenario 2, we perturb the initial guess of the wall and jacket temperature profile by a Gaussian zero-mean disturbance with a standard deviation of 20 °C. In both scenarios, we also perturb the initial guess of the heat transfer coefficients by +50%. The results are presented in Figs. 7 and 8. In the top graph of Fig. 7 we can observe that the estimator is able to converge to the true value of the heat transfer coefficients (in this graph we only present the value of the first reaction zone in scenario 1). In the middle graph, note that the initial guess of the wall temperature profile in scenario 1 is shifted and the estimator is able to converge to the true wall temperature profile at sampling time t_5. In the bottom graph, we note the large disturbances added to the initial guess of the wall profile in scenario 2. The estimator is also able to reconstruct the true wall temperature profile at around time t_5.

In the top graph of Fig. 8 we demonstrate that the estimator also converges to the true jacket temperature profile. In the middle graph, we can observe that the available temperature measurements provide enough information to reconstruct the concentration of radicals across the reactor at the first sampling time t_1. Here, it is also possible to identify the addition of initiator flow rates at the beginning of each reaction zone and the fast consumption. In the bottom graph of Fig. 8 we see that the temperature profile provides enough information to infer quickly the polymer melt index at reactor outlet. These results are quite surprising as in many processes temperature measurements are not sufficient to infer all the model states. In contrast, it seems that the *shape* of the temperature profiles arising in LDPE reactors presents a significant
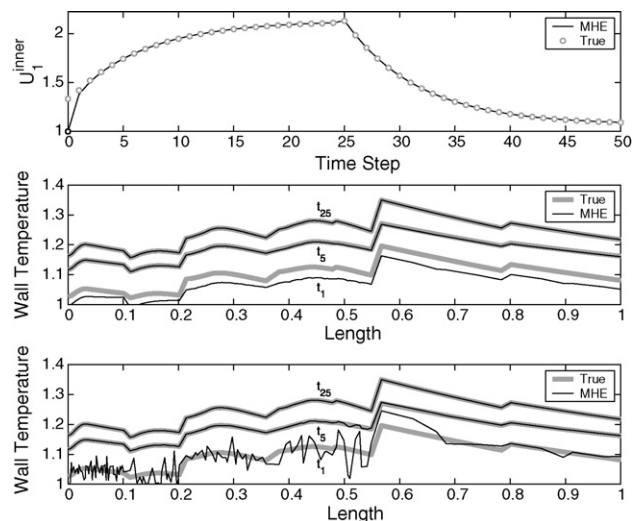

Fig. 7. Convergence properties of MHE estimator for perturbations on initial guess. Convergence to heat transfer coefficient of first reaction zones in scenario 1 (top). Convergence to wall temperature profile in scenario 1 (middle) and scenario 2 (bottom).

degree of *excitation* at each reaction zone that tends to make the data highly informative.

The solution of all the NLPs (7) considered satisfy second order conditions indicating that the process is observable under the available measurement information. To quantify the observability properties of the reactor, we perform a numerical analysis of the covariance matrix of the estimated wall temperature profile ($\mathbf{\Pi}_N$) for different values of the estimation horizon N. The results are presented in Fig. 9. In the top graph, we plot the diagonal elements of the covariance matrix corresponding to each wall temperature along the reactor. As a first observation, it is clear that the wall temperature can be inferred more reliably close to the reactor inlet (smaller covariance values) than downstream of the reactor. In addition, note that the levels of the covariance profiles decay quickly as the estimation horizon is increased. In the bottom graph, we plot the maximum eigenvalue of the covariance
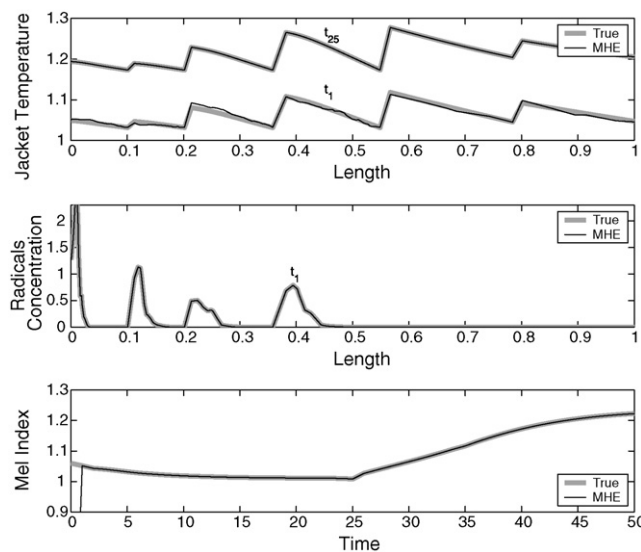

Fig. 8. Convergence properties of MHE estimator for perturbations on initial guess. Convergence to jacket temperature profile in scenario 1 (top). Convergence to radicals concentration profile at time step t_1 (middle). Convergence to polymer melt index at the reactor outlet (bottom).
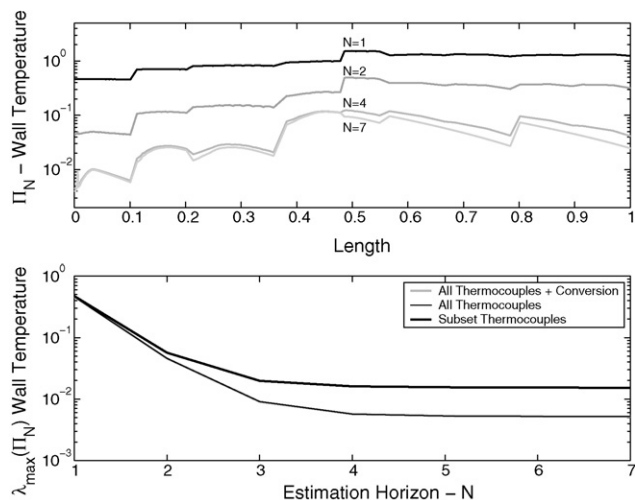
Fig. 9. Effect of estimation horizon length on convergence of estimator. Covariance of wall temperature profiles for different horizon lengths N (top). Decay of maximum eigenvalue of covariance matrix for different measurement scenarios (bottom).

Fig. 10. Effect of output noise on performance of estimator. Output noise on reactor core temperature with $\sigma = \pm 3\,°C$ and convergence to heat transfer coefficients (top). Output noise with $\sigma = \pm 5\,°C$ and corresponding heat transfer coefficients (bottom).

matrix $\lambda_{\max}(\mathbf{\Pi}_N)$ as a function of the estimation horizon. We compare three cases. The first case involves the estimator using the full measurement information available (core and jacket temperatures, inputs and conversion). The profile is presented as a solid gray line. Note that the maximum eigenvalue decays very quickly as the horizon length is increased. Five time steps seem to be sufficient to obtain a reliable estimate of the wall profile. In the second case, we eliminate the conversion measurement from the objective function (dashed black line). Note that the covariance of the wall profile is not affected by this modification, implying that the conversion measurement is redundant. In the third case, we eliminate one third of the reactor core measurements distributed along the reactor. Note that this change strongly affects the covariance of the estimated states. This demonstrates the crucial role that the temperature profile plays on the observability properties of the reactor.

5.1.2. Output noise filtering

We demonstrate the performance of the estimator for cases in which random Gaussian noise is added to the temperature measurements. In the first scenario, we add noise with a standard deviation $\sigma = \pm 3\,°C$ to each thermocouple measurement. This is a fairly standard noise level encountered in industrial reactors. In the second scenario we increase the level of noise to $\pm 5\,°C$. In both scenarios, the corresponding diagonal elements of the covariance matrix $\mathbf{R}$ are set to $(1/\sigma^2)$. The results are presented in Fig. 10. As can be seen, the estimator is able to reject the measurement noise and reconstruct the profile of the heat transfer coefficients.

5.1.3. Input noise filtering

It is well-known that input measurement noise leads to biased state estimates. To illustrate this, we consider the scenario in which the inlet temperature of the cooling water of all the zones is contaminated with Gaussian noise with $\sigma = \pm 3\,°C$. The results are presented in Fig. 11. In the top graph, we illustrate the inlet cooling water temperature corrupted with noise. In the middle graph, we can see that the input noise disrupts the convergence of the estimator to the true jacket temperature profile at time t_{50} (top graph). The estimate is biased. In the bottom graph, we observe that input noise also degrades the convergence of the estimator to the true heat transfer coefficients.
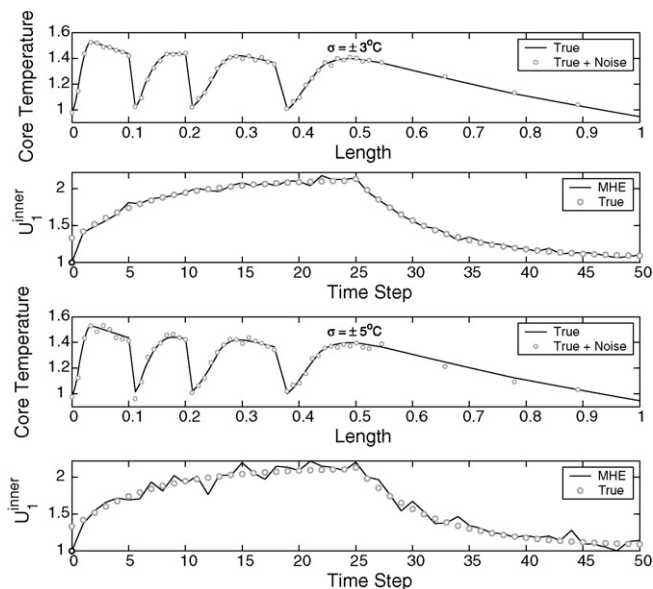
In order to filter input noise, the values of the input variables can be reconciled simultaneously in the estimator formulation. In parameter estimation literature, this is known as an errors-in-variables-measured (EVM) formulation. While this approach presents many advantages, it has been traditionally avoided in large-scale applications as it gives rise to optimization problems with many degrees of freedom (e.g. all side stream flow rates and temperatures along the reactor zones). In the proposed computational strategy, we are able to handle a relatively large number of degrees of freedom. This has enabled us to analyze the potential benefits of EVM-MHE formulations. In order to do this, we corrupt the measurements of the inlet cooling water temperatures with Gaussian noise with $\sigma = \pm 3\,°C$. Accordingly, we define all these inputs as degrees of freedom in the NLP. In addition, we incorporate the corresponding least-squares terms to the objective function
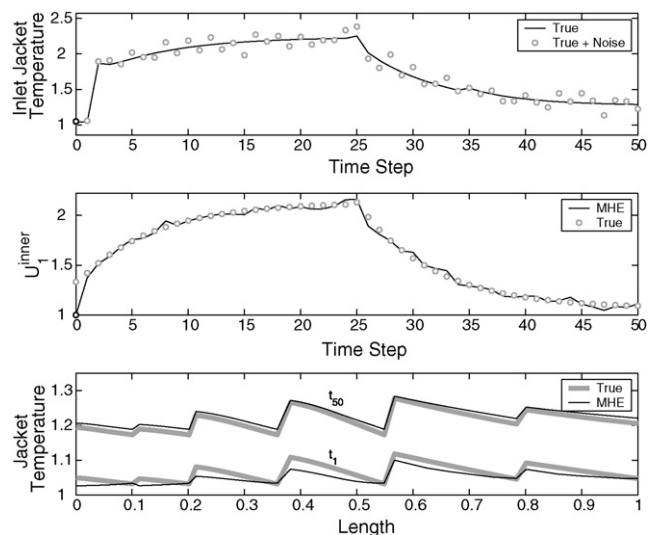

Fig. 11. Effect of *unrejected* input noise on performance of estimator. True and noisy jacket inlet temperatures for Zone 1 (top). Estimated heat transfer coefficient for Zone 1 (middle). Biased estimates of wall temperature profile (bottom).

Fig. 12. Effect of *rejected* input noise on performance of estimator. True, reconciled and noisy jacket inlet temperatures for Zone 1 (top). Estimated heat transfer coefficient for Zone 1 (middle). Unbiased estimates of wall temperature profile (bottom).
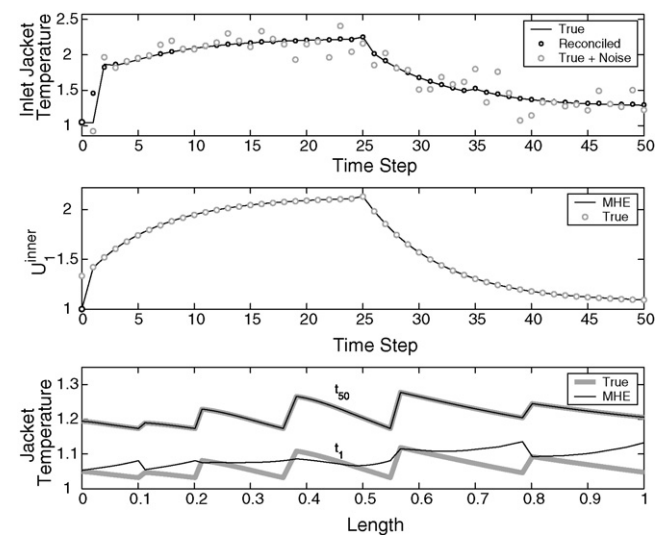
and modify the corresponding diagonal elements of the covariance matrix **R**. In the top graph of Fig. 12, we can see that the estimator is able to filter out the input noise and infer the true input. In the middle graph, we see the resulting smoother convergence of the heat transfer coefficients to the true value, compared to those observed in Fig. 11. In the bottom graph, we see the bias elimination on the jacket temperature profile through the EVM formulation.

5.2. Computational results

In Table 2, we present some characteristics of the NLPs resulting from the full discretization of the MHE problem and corresponding average solution times. All numerical calculations were performed on a 64-bit Sun Workstation with a Dual-Core processor running at 2.4 GHz. Linux is the operating system. The IPOPT solver is run with a fixed barrier parameter of 1×10^{-6} and the tolerance is set to 1×10^{-3}. We use the default preordering strategy (approximate minimum degree ordering-AMD) in MA57 during the factorization of the KKT matrix.

As an example, we consider a *standard* MHE problem with an horizon of 5 time steps and where the discretized initial profiles of the wall and jacket temperatures and the heat transfer coefficients are the degrees of freedom (DOF). The resulting NLP problem contains 40,390 constraints, 528 DOF and 4310 variable bounds. An NLP with these characteristics converges in 4 iterations and takes
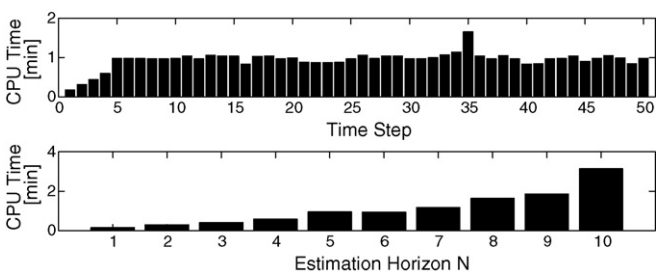

Fig. 13. History of solution times for average MHE problem with 5 time steps and 528 degrees of freedom (top). Average solution times as a function of the horizon length for standard MHE formulation (bottom).

around one minute. In the top graph of Fig. 13, we illustrate the solution time history for a particular MHE scenario. The largest problem solved using the *standard* MHE formulation contains an horizon of 10 time steps, 80,780 constraints and 648 DOF. On average, this problem can be solved in 4 iterations and 3 min. Based on these results, it is clear that the implementation of the MHE strategy is computationally feasible.

For the EVM-MHE formulations, the number of DOF increases with the estimation horizon. From Table 2, it is interesting to observe that the number of iterations taken by the NLP solver is not affected by this. This is a direct consequence of using exact second derivative information to compute the Newton steps. Nevertheless, an unexpected result is that the solution time of the EVM problems increases significantly with the size of the estimation horizon. In particular, notice that the EVM problem with an horizon of 8 time steps takes around 17 min to solve (around 4.5 min per iteration). However, note that the number of DOF in the standard counterpart is already very large and the problem can be solved in less than 2 min. From this observation, it seems that the number of DOF is not *per se* the source of the increase in the computational cost. In this case, the difference can be attributed to structural changes of the KKT matrix due to the addition of certain DOF such as the initiator flow rates and inlet temperatures. These structural changes seem to make the factorization of the KKT matrix more expensive to the linear solver, compared to the standard MHE formulation. In particular, it was found that the AMD preordering strategy is not able to account for these structural changes efficiently. For instance, for a standard MHE problem with an estimation horizon of 5 time steps, the number of nonzero entries in the KKT matrix is 636,185. After factorization with AMD preordering, the number of nonzero elements increases to 7,478,625. This gives a fill-in ratio of $7,478,625/636,185 \approx 11.75$. For an EVM-MHE problem with the same estimation horizon, the sparsity of the KKT matrix is similar (659,618 nonzero entries). However, the number of nonzero entries

Table 2
Characteristics of NLP problems and average solution times.

Horizon N	Type	Constraints	DOF	Total time [s]	Iterations	Time/iteration [s]
1	Standard	8078	432	8.707	4	2.17
1	EVM	8142	457	9.175	4	2.29
3	Standard	24234	480	23.83	4	5.95
3	EVM	24426	555	28.81	4	7.20
5	Standard	40390	528	56.76	4	14.90
5	EVM	40710	653	143.38	4	35.84
8	Standard	64624	600	97.69	4	24.42
8	EVM	65136	800	1064.57	4	266.14
10	Standard	80780	648	188.21	4	47.05
10	EVM	81420	898	3079.45	4	769.86

AMD preordering strategy used for factorization of KKT matrix.

Table 3
Solution times of EVM problems using AMD and ND preordering strategies.

Horizon N	Total time AMD [s]	Total time ND [s]
1	9.175	8.46
3	28.81	24.61
5	143.38	39.91
8	1064.57	81.54
10	3079.45	126.69
15	–	223.36
20	–	263.83

in the factors increases significantly (12,313,932). In other words, for two NLPs with nearly the same dimensions, the addition of particular variables as DOF can nearly double the fill-in ratio and thus increase the solution time by a factor of 2 or more.

Motivated by the rather poor performance of the AMD reordering in the EVM problems, we tested the performance of the nested dissection (ND) preordering strategy. The total solution times for ND are contrasted against those of AMD in Table 3. All problems were solved in 4 iterations. The solution times clearly illustrate the superiority of the ND preordering in identifying the structural changes of the EVM formulation. In particular, the solution time of an EVM problem with 10 time steps can be reduced by a factor of 30. In addition, note that the total solution times of ND strategy in the EVM problems are shorter than those of the AMD for the standard MHE formulation of Table 2. The largest EVM problem solved with ND contains 20 time steps in the estimation horizon. This corresponds to an NLP with 162,840 constraints and 1388 DOF that can be solved in around 4 min. From these results it is possible to conclude that the ND strategy is, in general, much more efficient in exploiting the structure of the KKT matrix.

6. Conclusions and future work

In this work, we have presented a computational strategy that allows the implementation of moving horizon estimation (MHE) strategies in low-density polyethylene (LDPE) tubular reactors. The estimator is built around a detailed dynamic model of the reactor described by large sets of nonlinear partial, differential and algebraic equations. To solve the resulting large-scale MHE problem, we follow a full discretization approach. This results in a sparse nonlinear programming (NLP) problem that can be solved with state-of-the art NLP solvers. The practical benefits of the MHE estimator are demonstrated in an industrial scenario arising in the operation of LDPE reactors. It was found that limited temperature measurements distributed along the reactor provide sufficient information to infer all the model states and to track time-varying fouling phenomena. The estimator exhibits strong convergence properties, recovers from poor initial guesses of the states and parameters and requires relatively short estimation horizons. In addition, we demonstrate the potential benefits of using errors-in-variables-measured (EVM) formulations to filter out output and input measurement noise simultaneously through the MHE estimator. Finally, we demonstrate that the implementation of these strategies is computationally feasible.

As part of future work, we plan to embed the estimator within a Nonlinear Model Predictive Control (NMPC) application to optimize the operation of LDPE reactors. For this, we will accommodate the MHE estimator in a real-time environment by making use of recently proposed on-line synchronization strategies (Zavala et al., 2007, in press). These strategies shift the solution time of the MHE problem to the background period between sampling times and thus allow to obtain nearly instantaneous state estimates that can be used to compute fast control actions. Finally, an interesting area of future research is the consideration of advanced MHE formulations able to account for gross errors and process noise.

References

Alessandri, A., Baglietto, M., & Battistelli, G. (2008). Moving-horizon state estimation for nonlinear discrete-time systems: New stability results and approximation schemes. *Automatica*, *44*, 1753–1765.

Bard, Y. (1974). *Nonlinear parameter estimation*. Cambridge, MA: Academic Press.

Benson, H. Y., Shanno, D. F., & Vanderbei, R. J. (2002). Interior-point methods for nonconvex nonlinear programming: Filter methods and merit functions. *Computational Optimization and Applications*, *23*, 257–272.

Biegler, L. T., Cervantes, A. M., & Wächter, A. (2002). Advances in simultaneous strategies for dynamic process optimization. *Chemical Engineering Science*, *57*, 575–593.

Bokis, C. P. (2001). Physical properties, reactor modeling, and polymerization kinetics in the low-density polyethylene tubular reactor process. *Industrial & Engineering Chemistry Research*, *41*, 1017–1030.

Brandolin, A., Lacunza, P., Ugrin, L., & Capiati, N. J. (1996). High-pressure polymerization of ethylene and improved mathematical model for industrial tubular reactors. *Polymer Reaction Engineering*, *4*, 193–241.

Buchelli, A., Call, M. L., Brown, A. L., Bird, A., Heard, S., & Hannon, J. (2005a). Modeling fouling effects in LDPE tubular polymerization reactors. 1. Fouling thickness determination. *Industrial & Engineering Chemistry Research*, *44*, 1474–1479.

Buchelli, A., Call, M. L., Brown, A. L., Bird, A., Heard, S., & Hannon, J. (2005b). Modeling fouling effects in LDPE tubular polymerization reactors. 2. Heat transfer, computational fluid dynamics and phase equilibria. *Industrial & Engineering Chemistry Research*, *44*, 1480–1492.

Byrd, R. H., Gilbert, J. Ch., & Nocedal, J. A. (2000). Trust-region method based on interior-point techniques for nonlinear programming. *Mathematics Programming*, *89*, 149–185.

Diehl, M., Bock, H. G., & Schlöder, J. P. (2005). A real-time iteration scheme for nonlinear optimization in optimal feedback control. *SIAM Journal on Control and Optimization*, *43*, 1714–1736.

Duff, I. S. (2004). MA57—A code for the solution of sparse symmetric definite and indefinite systems. *ACM Transactions on Mathematical Software*, *30*, 118–144.

Fourer, R., Gay, D. M., & Kernighan, B. W. (1992). *AMPL: A modeling language for mathematical programming*. Belomont, CA: Duxbury Press.

Goto, S., et al. (1981). Computer model for commercial high-pressure polyethylene reactor based on elementary reaction rates obtained experimentally. *Journal of Applied Polymer Science*, *36*, 21–40.

Häfele, M., Kienle, A., Boll, M., & Schmidt, C. U. (2006). Modeling and analysis of a plant for the production of low density polyethylene. *Computers & Chemical Engineering*, *31*, 51–65.

Haseltine, E. L., & Rawlings, J. B. (2005). Critical evaluation of extended kalman filtering and moving horizon estimation. *Industrial & Engineering Chemistry Research*, *44*, 2451–2460.

Karypis, G., & Kumar, V. (1999). A Fast and high quality multilevel scheme for partitioning irregular graphs. *SIAM Journal on Scientific Computing*, *20*, 359–392.

Kim, D. M., & Iedema, P. D. (2004). Molecular weight distribution in low-density polyethylene polymerization: Impact of scission mechanisms in the case of a tubular reactor. *Chemical Engineering Science*, *59*, 2039–2052.

Kiparissides, C., Verros, G., & McGregor, J. (1993). Mathematical modeling, optimization and quality control of high-pressure ethylene polymerization reactors. *Journal of Macromolecular Science, Part C: Polymer Reviews*, *33*, 437–527.

Kiparissides, C., Verros, G., Pertsinidis, A., & Goosens, I. (1996). On-line parameter estimation in a high-pressure low-density polyethylene tubular reactor. *AICHE Journal*, *42*, 440.

Kiparissides, C., Baltsas, A., Papadopoulos, S., Congalidis, J. P., Richards, J. R., Kelly, M. B., et al. (2005). Mathematical modeling of free-radical ethylene copolymerization in high-pressure tubular reactors. *Industrial & Engineering Chemistry Research*, *44*, 2592–2605.

Knuuttila, H., Lehtinen, A., & Nummila-Pakarinen, A. (2004). Advanced polyethylene technologies: Controlled material properties. *Advances in Polymer Science*, *169*, 13–27.

Lacunza, M., Ugrin, P. E., Brandolin, A., & Capiati, N. J. (1998). Heat transfer coefficient in a high pressure tubular reactor for ethylene polymerization. *Polymer Engineering & Science*, *38*, 992–1013.

Luft, G., Bitsch, H., & Seidl, H. (1977). Effectiveness of organic peroxide initiators in the high-pressure polymerization of ethylene. *Journal of Macromolecular Science: Chemistry*, *A11*, 1089–1112.

Nocedal, J., & Wright, S. J. (1999). *Numerical optimization*. New York: Springer-Verlag.

Pertsinidis, A., Papadopoulos, E., & Kiparissides, C. (1996). Modeling and analysis of a plant for the production of low density polyethylene. *Computers & Chemical Engineering*, *20*, S449–S454.

Rawlings, J. B., & Bakshi, B. R. (2006). Particle filtering and moving horizon estimation. *Computers & Chemical Engineering*, *30*, 1529–1541.

Wächter, A., & Biegler, L. T. (2006). On the implementation of an interior-point filter line-search algorithm for large-scale nonlinear programming. *Mathematical Programming*, *106*, 25–57.

Zabisky, R. C. M., Chan, W. M., Gloor, P. E., & Hamielec, A. E. (1992). A kinetic model for olefin polymerization in high-pressure tubular reactors. A review and update. *Polymer*, *33*, 2243–2262.

Zavala, V. M., & Biegler, L. T. (2006). Large-scale parameter estimation in low-density polyethylene tubular reactors. *Industrial & Engineering Chemistry Research*, *25*, 7867–7881.

Zavala, V. M., & Biegler, L. T. (2008). Large-scale nonlinear programming strategies for the operation of low-density polyethylene tubular reactors. In *Proceedings of ESCAPE 18* Lyon, France.

Zavala, V. M., Laird, C. D., & Biegler, L. T. (2007). A Fast Computational Framework for Large-Scale Moving Horizon Estimation. In *Proceedings of 8th International Symposium on Dynamics and Control of Process Systems* Cancun, Mexico.

Zavala, V. M., Laird, C. D., & Biegler, L. T. (2008). A moving horizon estimation algorithm based on nonlinear programming sensitivity. *Journal of Process Control*, *18*, 876-884.